Energy & Environmental Science

ROYAL SOCIETY OF CHEMISTRY

PAPER

View Article Online
View Journal

Cite this: DOI: 10.1039/d5ee03005f

Central core asymmetric acceptor design enables over 20% efficiency in binary organic solar cells by suppressing non-radiative energy loss and optimizing nanomorphology

Jian Liu,†[a] Zhaochen Suo,†[a] Longyu Li,[a] Wenkai Zhao,[b] Jingyi Huo,[a] Jiye Chen,[a] Guankui Long,[b] Zhaoyang Yao,[a] Chenxi Li,[a] Xiangjian Wan*[a] and Yongsheng Chen[a]

Asymmetric acceptors characterized by core asymmetry exhibit great potential for achieving outstanding efficiency, despite the limited number of relevant studies reported to date. In this work, we propose an asymmetric molecular design strategy that combines core asymmetric substitution with halogenation engineering to design and synthesize two acceptors, namely Ph-2F and Ph-2Cl. The two acceptors showed high photoluminescence quantum yields (PLQYs) induced by the asymmetric substitution central core, leading to a reduction in non-radiative energy loss. Meanwhile, the two acceptors demonstrate good miscibility and optimized morphology with the donor PM6. Consequently, the binary OSCs based on PM6:Ph-2F and PM6:Ph-2Cl achieved high power conversion efficiencies (PCEs) of 20.33% (certified 19.70%) and 19.13%, respectively. Note that the efficiency of 20.33% is the highest value reported for asymmetric acceptor-based binary OSCs so far. Remarkably, an outstanding PCE of 17.16% was obtained in a 13.5 cm^2 module, the highest value reported for binary OSC modules to date. Our work highlights the great potential of core-asymmetry molecular design strategies in improving device performance.

Received 31st May 2025,
Accepted 8th August 2025

DOI: 10.1039/d5ee03005f

rsc.li/ees

Broader context

Although power conversion efficiencies (PCEs) of organic solar cells (OSCs) have exceeded 20%, most of them are fabricated using a ternary active layer in order to balance the three parameters, V_{OC}, J_{SC} and FF. Only a few cases of binary devices with PCEs over 20% are reported. Compared to ternary devices, binary devices show many advantages such as simpler morphology control, lower processing complexity and better reproducibility, providing more opportunities for the future application of OSCs. Asymmetric acceptors usually exhibit great structural adjustability, which is expected to achieve outstanding efficiencies. However, most studies on asymmetric acceptors primarily focus on terminal groups and side chains, while few research studies on core-asymmetry have been reported so far. In this work, we design two core-asymmetric acceptors Ph-2F and Ph-2Cl. This core-asymmetric grafted substation effectively suppresses non-radiative energy loss and optimizes nanomorphology, thereby achieving high V_{OC} without compromising J_{SC} and FF, and thus enhancing the efficiency of binary OSCs. Thus, PM6:Ph-2F and PM6:Ph-2Cl based devices achieved PCEs of 20.33% and 19.13%, respectively. Note that 20.33% efficiency is the highest value among the binary devices based on asymmetric acceptors to date. Furthermore, an outstanding PCE of 17.16% was obtained in a 13.5 cm^2 module.

Introduction

Organic solar cells (OSCs) have attracted increasing attention due to their merits, including solution-processability, low-cost, light-weight, flexibility and transparency.[1–7] Benefiting from the rapid development of active layer materials and device fabrication technology, OSCs have made great advancement with power conversion efficiencies (PCEs) exceeding 20%.[8–12] PCEs of OSCs are determined by three parameters: short-circuit current density (J_{SC}), fill factor (FF) and open-circuit voltage

[a] State Key Laboratory of Elemento-Organic Chemistry, Frontiers Science Center for New Organic Matter, The Centre of Nanoscale Science and Technology and Key Laboratory of Functional Polymer Materials, Institute of Polymer Chemistry, Renewable Energy Conversion and Storage Center (RECAST), Tianjin Key Laboratory of functional polymer materials, Nankai University, Tianjin, 300071, China. E-mail: xjwan@nankai.edu.cn

[b] School of Materials Science and Engineering, National Institute for Advanced Materials, Renewable Energy Conversion and Storage Center (RECAST), Nankai University, Tianjin, 300350, China

† These authors contributed equally.

(V_{OC}). J_{SC} and FF are closely related to the blend nanomorphology, while V_{OC} is limited by the energy loss (E_{loss}), particularly non-radiative energy loss (ΔE_{nr}). To achieve high efficiency, it is necessary to improve the above three parameters simultaneously. However, it is still challenging to this end in materials design and device optimization. Although many devices with efficiencies over 20% have been reported, most of them are fabricated using a ternary active layer in order to get the three balanced parameters. Only a few cases of binary devices with efficiencies over 20% have been reported.[13–15] In fact, compared to the ternary device, binary devices have many advantages *e.g.* simpler morphology control, lower processing complexity and better reproducibility, which provide more opportunities for the application of OSCs in the future. Therefore, it is urgent and necessary to design active layer materials for efficient binary devices.

Recent research has demonstrated that asymmetric acceptors usually exhibit great structural adjustability, which is excepted to simultaneously improve the three photovoltaic parameters.[16–18] Currently, most studies on asymmetric acceptors primarily focus on modifications to the terminal groups and side chains,[19–24] while asymmetry in the central core remains significantly underexplored.[25–27] Moreover, many of the asymmetrical acceptors reported so far rely on ternary strategies to attain high PCEs, which adds complexity to device fabrication and operation. In contrast, the binary device PCEs of asymmetric acceptors still lag behind those of their symmetric counterparts. Therefore, it is crucial to develop simple yet effective molecular design strategies targeting core asymmetry to synergistically reduce ΔE_{nr} and optimize nanomorphology, thereby achieving high V_{OC} without compromising J_{SC} and FF, and thus enhancing the efficiency of binary OSCs.

In this work, we designed two core-asymmetric acceptors, namely Ph-2F and Ph-2Cl *via* combining core asymmetric substitution with the grafted and halogenated benzene unit. This grafted asymmetric substation not only effectively improves the luminescence properties of the two acceptors and suppresses ΔE_{nr}, but also regulates the donor–acceptor interaction and optimizes active layer morphology, ultimately achieving high device performance. As a result, the PM6:Ph-2F- and PM6:Ph-2Cl-based binary devices achieved high PCEs of 20.33% and 19.13%, respectively. Particularly, the 20.33% efficiency is the highest value reported for asymmetric acceptor-based OSCs so far. Besides, based on the superior performance of small devices, an outstanding PCE of 17.16% was obtained in a 13.5 cm^2 module, which is the highest value reported for binary OSCs to date. This work demonstrates the potential of core-asymmetric acceptors to exceed the 20% PCE threshold, offering a promising strategy for the design of high-efficiency acceptors.

Results and discussion

The molecular structures of Ph-2F and Ph-2Cl are shown in Fig. 1a, and the detailed synthetic route can be found in the SI (Scheme S1). The two acceptors were characterized by ^{1}H NMR, ^{13}C NMR and high-resolution mass spectrometry (HRMS) (Fig. S1–S14). In order to reveal the effect of asymmetric molecular design strategy on the electronic properties of molecules, molecular surface electrostatic potential (ESP) distribution was calculated by density functional theory (DFT) at the B3LYP/6-31G* level (Fig. 1b). The color variation in the ESPs mainly focus on the halogenated-substituted benzenes located

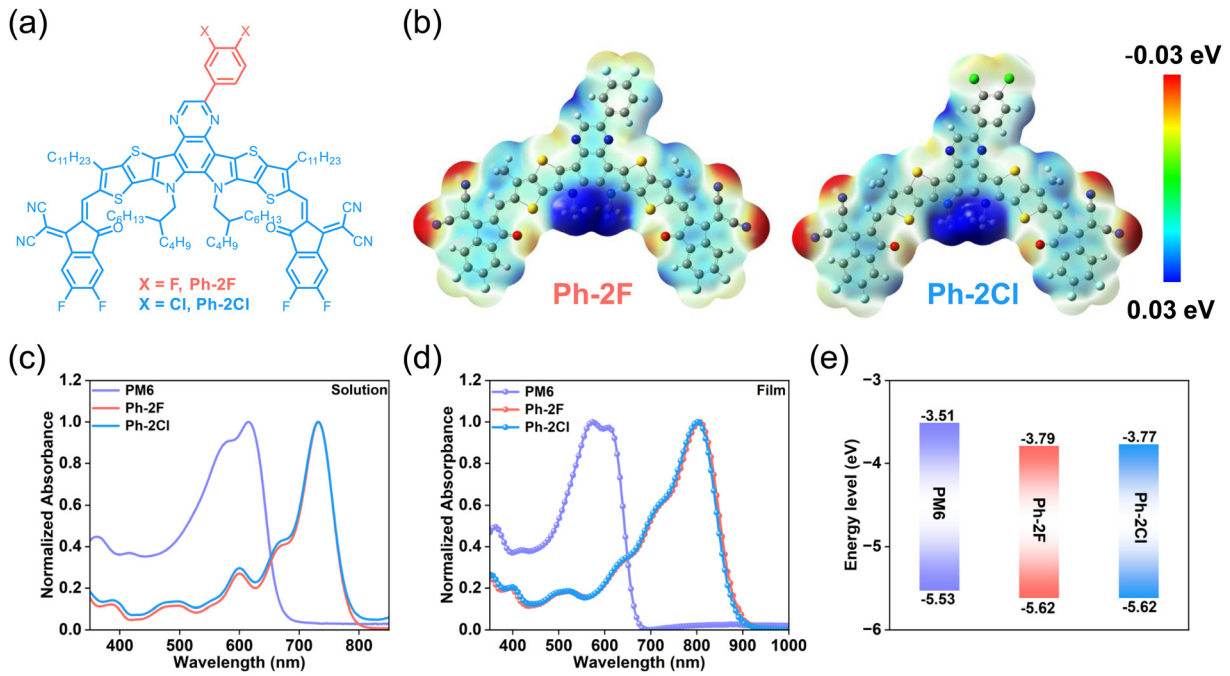

Fig. 1 (a) Chemical structures of Ph-2F and Ph-2Cl. (b) Electrostatic surface potential (ESP) of Ph-2F and Ph-2Cl. Normalized UV-vis absorption spectra of diluted solution (c) and pristine film (d) for Ph-2F and Ph-2Cl. (e) Energy level diagram of PM6, Ph-2F and Ph-2Cl films derived from CV tests.

at central cores, while the difference can be ignored in the terminal groups. The positive ESP values were mainly distributed on the molecular conjugate skeleton, while negative sections were concentrated on the carbonyl and cyano groups of the terminal units. In particular, Ph-2Cl has a slightly higher average ESP value of 5.11 kcal mol^{-1} compared to the value for Ph-2F of 4.98 kcal mol^{-1}, demonstrating that Ph-2Cl will have enhanced intermolecular interactions with the donor (Fig. S15).[28,29]

The normalized ultraviolet-visible (UV-vis) absorption spectra of the two acceptors in diluted chloroform solution and pristine film are depicted in Fig. 1c, d and Fig. S16, S17, and the relevant data are summarized in Table 1. Ph-2F and Ph-2Cl show same maximum absorption peaks (λ_{max}) in solution, due to their similar conjugated skeleton. Clearly a red-shift of λ_{max} can be observed from solution to solid film for the two acceptors. Specifically, Ph-2F and Ph-2Cl exhibit λ_{max} at 808 and 803 nm in film state, corresponding to the red-shifts of 76 and 71 nm, respectively. The larger red-shift observed in Ph-2F indicates a more pronounced π–π stacking compared to Ph-2Cl, primarily due to the increased electronegativity of fluorine atoms in the benzene ring positioned at the central pyrazine site.[30,31] In addition, we also conduct theoretical calculation to evaluate molecular dipole moments for the two acceptors, and the detailed results are shown in Fig. S18, S19 and Table S1. The $\Delta\mu_{ge}$ refers to the difference between ground-state dipole moment (μ_g) and excited-state dipole moment (μ_e), which can be calculated based on the margin of μ_g and μ_e along each axis.[32] Ph-2F has larger $\Delta\mu_{ge}$ values of 0.42 Debye than the value of 0.40 Debye of Ph-2Cl, indicating Ph-2F exhibits a stronger intermolecular interaction than Ph-2Cl, aligning with the UV-Vis measurement results discussed above.[33] This ensures Ph-2F has a higher electron–hole pair separation efficiency and faster charge transfer rate, contributing to achieving better photovoltaic performance.[34] As shown in Fig. S20, cyclic voltammetry measurement was conducted to investigate the energy levels for Ph-2F and Ph-2Cl in solid films, and the energy level diagram of polymer donor PM6 and the two acceptors is illustrated in Fig. 1e. Ph-2F shows the same HOMO energy level of −5.62 eV with Ph-2Cl, while there is a little difference in their LUMO energy levels (−3.79 eV for Ph-2F and −3.77 eV for Ph-2Cl).

To investigate the photovoltaic performance of the two asymmetric acceptors, OSCs were fabricated with a conventional structure of ITO/2PACz/PM6:Acceptors/PNDIT-F3N/Ag. Polymer PM6 was selected as the donor in the active layer due to its complementary absorption and matched energy levels with the two acceptors. The molecular structures of PM6, 2PACz and PNDIT-F3N are provided in the Fig. S21. Details of the device fabrication process are provided in the SI (Tables S2–S4). The current density–voltage (*J–V*) curves based on optimized devices are presented in Fig. 2a and the corresponding photovoltaic parameters are listed in Table 2. Notably, both binary OSCs exhibited a high V_{OC} exceeding 0.9 V. The Ph-2Cl-based device exhibited a PCE of 19.13% with a V_{OC} of 0.908 V, J_{SC} of 26.12 mA cm^{-2} and FF of 80.65%. In comparison, the PM6:Ph-2F binary device demonstrated an impressive PCE of 20.33% (certified 19.70%, Fig. S22), benefiting from simultaneous improvements in J_{SC} of 27.58 mA cm^{-2} and FF of 81.26% while maintaining a similar V_{OC} of 0.906 V, the highest PCE reported for binary OSCs based on asymmetric acceptors to date (Fig. 2b). Additionally, the PCE distribution box plots for 20 independent devices are shown in Fig. 2c, with detailed performance parameters provided in Tables S6 and S7. The Ph-2F-based devices exhibited a more concentrated and consistent PCE distribution, indicating better reproducibility compared to Ph-2Cl-based devices. Meanwhile, we also use D18 as a polymer donor to fabricate the corresponding binary devices, and the detailed device parameters are provided in the SI (Fig. S23 and Table S8). The D18:Ph-2F and D18:Ph-2Cl based devices exhibit PCEs of 19.81% and 18.65%, respectively. Based on the above results, our follow-up research mainly focuses on the PM6:Ph-2F and PM6:Ph-2Cl blend systems.

The external quantum efficiency (EQE) spectra of the optimal devices are shown in Fig. 2d. The PM6:Ph-2Cl device exhibits a moderate response in the range of 400–850 nm with an edge at 894 nm. In contrast, the PM6:Ph-2F-based device not only demonstrates a higher EQE response, but also features a red-shifted EQE curve edge, consistent with the result of the UV-Vis absorption spectra of the two blend films (Fig. S24). The enhanced EQE response and broader spectral coverage in Ph-2F-based devices can be attributed to the optimized phase separation morphology and improved exciton transport properties as discussed below. The J_{SC} values integrated from EQE curves for PM6:Ph-2F and PM6:Ph-2Cl based devices were 26.66 and 25.44 mA cm^{-2} respectively, demonstrating excellent reproducibility (Fig. S25), and showing good agreement with the *J–V* measurements. In addition, we also measured the photostability of the two binary devices under maximal power point (MPP) tracking conditions, and the detailed results are shown in Fig. S26. Note that the Ph-2F based device has a longer T_{80} lifetime of 403 h than the 304 h lifetime of the Ph-2Cl based device, indicating that the Ph-2F based device demonstrates better photostability than the Ph-2Cl based device.

In consideration of the superior performance of the Ph-2F-based small area device, we further fabricated a large-area module using a similar procedure. The detailed preparation process is provided in the SI. This module consists of six subcells connected in series with an effective area of 13.5 cm^2, and its photograph is depicted in Fig. S27. After primary optimization, the champion module achieved a remarkably record-

Table 1 The optical and electrochemical properties of Ph-2F and Ph-2Cl

Acceptors	λ_{max}^{sol} (nm)	λ_{max}^{film} (nm)	$\Delta\lambda$ (nm)	λ_{onset}^{film} (nm)	E_g^{opt} [a] (eV)	E_{HOMO} [b] (eV)	E_{LUMO} [b] (eV)
Ph-2F	732	808	76	886	1.40	−5.62	−3.79
Ph-2Cl	732	803	71	882	1.41	−5.62	−3.77

[a] Optical band gap was calculated by $1240/\lambda_{onset}^{film}$. [b] The highest occupied molecular orbital (HOMO) and lowest unoccupied molecular orbital (LUMO) energy levels were calculated from the onset oxidation potential and the onset reduction potential using the equation: $E_{HOMO} = -(4.80 + E_{ox}^{onset})$ eV, $E_{LUMO} = -(4.80 + E_{re}^{onset})$ eV.

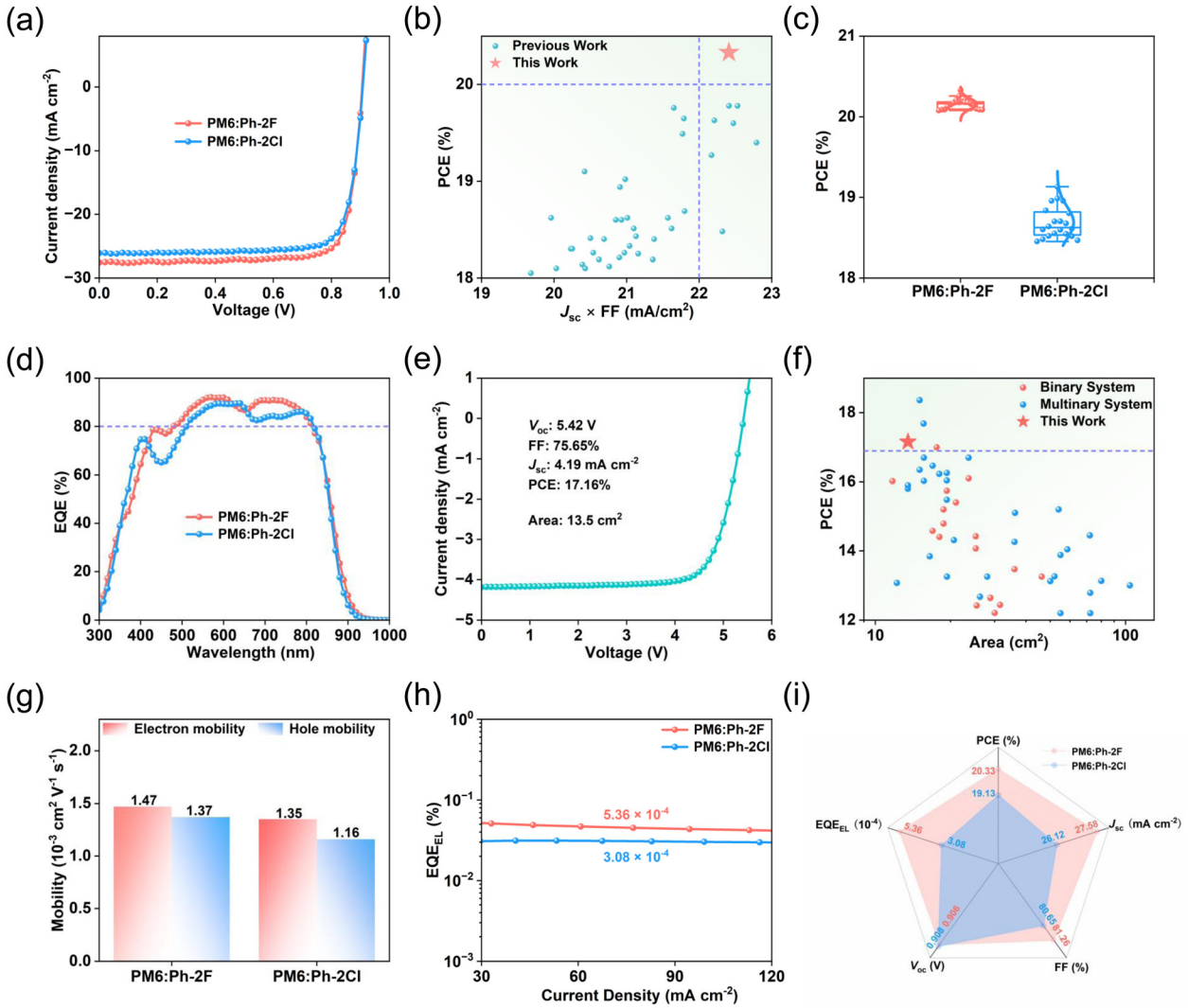

Fig. 2 (a) J–V curves of the optimal device based on PM6:acceptors. (b) Plots of the binary system PCE *versus* J_{SC} × FF for the asymmetrical acceptors reported in the literature with PCE > 18% and this work. Source references for the data points are provided in Table S5. (c) Box plots of the PCE distribution for devices under the corresponding conditions of AM 1.5 G and 100 mA cm^{-2}. (d) EQE curves of the optimal device based on PM6:acceptors. (e) The corresponding J–V curve of PM6:Ph-2F-based large-area OSC modules. (f) Plots of the PCE *versus* area for the OSC modules with an effective area over 10 cm^2 reported in the literature and this work. Source references for the data points are provided in Table S9. (g) Histograms of the hole and electron mobilities for the two blends acquired from single-carrier devices. (h) EQE$_{EL}$ spectra for the PM6:Ph-2F- and PM6:Ph-2Cl-based devices. (i) Comparison of critical performance parameters in the investigated binary OSCs.

Table 2 Summary of device parameters for optimized OSCs[a]

Active layers	V_{OC} (V)	J_{SC} (mA cm^{-2})	Cal. J_{SC}[b] (mA cm^{-2})	FF (%)	PCE (%)
PM6:Ph-2F	0.906 (0.903 ± 0.002)	27.58 (27.59 ± 0.19)	26.66	81.26 (80.87 ± 0.55)	20.33 (20.16 ± 0.06)
PM6:Ph-2Cl	0.908 (0.907 ± 0.002)	26.12 (25.81 ± 0.22)	25.44	80.65 (79.87 ± 0.84)	19.13 (18.69 ± 0.20)

[a] The average parameters afforded by 20 independent devices. [b] Current densities calculated from EQE curves.

breaking PCE of 17.16%, with a V_{OC} value of 5.42 V, a J_{SC} value of 4.19 mA cm^{-2} and an FF of 75.65%, as plotted in Fig. 2e. By summarizing the previous work *via* plotting module PCE *versus* area, our work represents the highest efficiency for binary OSC modules to date (Fig. 2f).

A series of tests were carried out to investigate the charge transfer, exciton dissociation and charge recombination properties for the two blends. The charge transport properties of the two blend films were measured by space-charge-limited current (SCLC) method in the electron-only and hole-only devices, as shown in Fig. 2g and Fig. S28. The detailed calculation method of electron mobility (μ_e) and hole mobility (μ_h) is provided in the SI, and the detailed values of μ_e/μ_h are 1.47/1.37 and 1.35/1.12 × 10^{-3} cm^2 V^{-1} s^{-1} for the Ph-2F- and Ph-2Cl-based blends (Table S10). All the

mobility values show good reproducibility for the two blends, which further ensure the reliability of the above results. The Ph-2F-based blend exhibits obviously enhanced charge mobilities with respect to the Ph-2Cl-based ones, and the higher mobilities in the Ph-2F-based blend are advantageous for its faster charge transport. Additionally, the Ph-2F-based blend shows a more balanced μ_e/μ_h ratio (1.07) than that of 1.16 for the Ph-2Cl-based blend, indicating suppressive recombination behavior in the Ph-2F-based blend. The higher mobilities and well balanced μ_e/μ_h ratio in the PM6:Ph-2F-blend are beneficial for simultaneously improving J_{SC} and FF, thus enable the champion device PCE of 20.33%.[35,36]

Transient photocurrent (TPC) and transient photovoltage (TPV) measurements were conducted to assess charge recombination behavior.[37,38] As shown in Fig. S29, the Ph-2F-based device has a similar rise process and faster decay process compared with the Ph-2Cl-based one, with a shorter charge extraction time of 0.47 μs (PM6:Ph-2F) than the 0.73 μs of PM6:Ph-2Cl by fitting TPC curves, indicating a more efficient and faster charge extraction process with fewer recombination in the PM6:Ph-2F system. Meanwhile, the Ph-2F-based device exhibits a longer charge lifetime of 68.4 μs than the Ph-2Cl-based one of 47.7 μs according to TPV curves, which coincides with the results of time-resolved photoluminescence (TRPL) measurement (Fig. S29). The pristine film of Ph-2F exhibits longer TRPL lifetimes of 1.27 ns than the 1.15 ns lifetime of the Ph-2Cl neat film, implying more efficient exciton dissociation in the donor/acceptor interface.[39] These results demonstrate that the Ph-2F-based device exhibits an improved charge transfer process coupled with less recombination behavior, leading to a synergistical enhancement of J_{SC} and FF.

In order to investigate the influence of asymmetric molecular design strategy on V_{OC}, we conducted energy loss (E_{loss}) analysis for the two devices following the established method.[40] According to the detailed-balanced theory, E_{loss} consists of three parts: $E_{loss} = E_g - qV_{OC} = (E_g - qV_{OC}^{SQ}) + (qV_{OC}^{SQ} - qV_{OC}^{rad}) + (qV_{OC}^{rad} - qV_{OC}) = \Delta E_1 + \Delta E_2 + \Delta E_3$, where E_g is the bandgap, ΔE_1 is the radiative loss above the bandgap,[41] and ΔE_2 and ΔE_3 are the radiative and non-radiative loss below the bandgap, respectively.[42–45] The detailed analysis data are summarized in Table S11. The E_g values of the two blend films were estimated *via* the intersection of normalized absorption and photoluminescence (PL) spectra, as plotted in Fig. S30. The E_g values are 1.447 and 1.453 eV for PM6:Ph-2F and PM6:Ph-2Cl, yielding the overall E_{loss} values of 0.541 and 0.545 eV, respectively.

A clear comparison of E_{loss} parameters is depicted in Fig. S31. The two devices show similar ΔE_1 ($\sim$0.266 eV) and ΔE_2 ($\sim$0.06 eV) values. As for ΔE_3, also known as ΔE_{nr}, it can be calculated by the equation of $\Delta E_3 = -kT\ln(EQE_{EL})$, where k is the Boltzmann constant, T is Kelvin temperature, and EQE_{EL} is the electroluminescence external quantum efficiency. The Ph-2F- and Ph-2Cl-based devices exhibit EQE_{EL} values of 5.36×10^{-4} and 3.08×10^{-4}, corresponding to the ΔE_3 values of 0.193 and 0.207 eV, respectively (Fig. 2h), which are much lower than many Y-series acceptors, *e.g.* Y6 and L8-BO based devices.[46,47] As reported by Gao *et al.*, enhanced luminescent properties of the low band gap component in the active layer is beneficial for suppressing ΔE_3 in OSCs.[48] Therefore, we conduct the PLQY measurements for Ph-2F, Ph-2Cl, Y6 and L8-BO under identical conditions, as shown in Fig. S32. In our results, Ph-2F, Ph-2Cl, Y6 and L8-BO exhibit PLQY values of 10.36%, 7.73%, 6.36% and 6.45%, respectively. The higher PLQY values of Ph-2F and Ph-2Cl correspond to the lower ΔE_3 observed in the PM6:Ph-2F and PM6:Ph-2Cl binary devices. Based on the above analysis, the Ph-2F-based device balances the $J_{SC} \times$ FF and V_{OC} with suppressed ΔE_3, thereby achieving an excellent PCE over 20%, highlighting the great potential of asymmetric acceptors in realizing high-performance OSCs (Fig. 2i).

The HOMO and LUMO energy level offsets significantly influence hole and charge transfer, respectively. Currently, the LUMO energy offsets between most donor and acceptor materials can provide enough driving force to charge transfer.[49] Therefore, hole transfer has become the decisive factor in determining the carrier transport process for NFA-based OSCs. Therefore, femtosecond transient absorption (fs-TA) spectroscopy measurement was applied to analyze the hole transfer process at the donor–acceptor (D–A) interface in the two systems, and the corresponding results are shown in Fig. 3 and Fig. S33–S37. As shown in Fig. 3a and d, when acceptors were selectively excited by a wavelength at 800 nm, the ground-state bleach (GSB) signals and excited-state absorption (ESA) signals appear at 820 nm and 905 nm, respectively. Note that Ph-2F exhibits a more obvious GSB peak with negative signal and ESA peak with positive signal compared to the Ph-2Cl neat film, which is consistent with the variation trend of the corresponding signals observed from the blend film.

When blended with the donor PM6, a new negative signal peak located at 630 nm appears in the 2D TA spectra (Fig. 3b and e), which can be assigned to the GSB signal peak of PM6. The decay of the acceptor GSB signal accompanied by the enhancement of donor GSB signal demonstrates the occurrence of efficient photoexcited hole transportation from acceptor to donor.[50] Furthermore, the GSB signal of the donor at 630 nm was extracted and fitted to evaluate the hole transfer dynamics, as illustrated in Fig. 3c, f and Table S12. Two vital parameters τ_1 and τ_2 reflect different sections of the hole transfer process respectively, where τ_1 represents the time required for exciton dissociation at the interface and τ_2 can be attributed to the exciton diffusion process from the intradomain to interface. It is clear that the PM6:Ph-2F blend film showed smaller τ_1 (0.121 ± 0.006 ps) and τ_2 (5.161 ± 0.229 ps) fitted values in comparison with the PM6:Ph-2Cl-based one ($\tau_1 = 0.288 \pm 0.080$ ps, $\tau_2 = 11.781 \pm 0.563$ ps), demonstrating that faster exciton dissociation and diffusion occur in the PM6:Ph-2F system along with suppressive recombination. Furthermore, photoluminescence (PL) quenching measurements were performed to quantitatively evaluate the hole transfer efficiency for the two blends (Fig. S38). The Ph-2F-based device give a higher PL quenching efficiency of 98.71% than those in the Ph-2Cl blend (97.38%). The superior PL quenching efficiency of 98.71% confirms that the Ph-2F blend film possesses high hole transfer efficiency, which is consistent with the TA results and ultimately leads to the promotion of J_{SC} and FF.

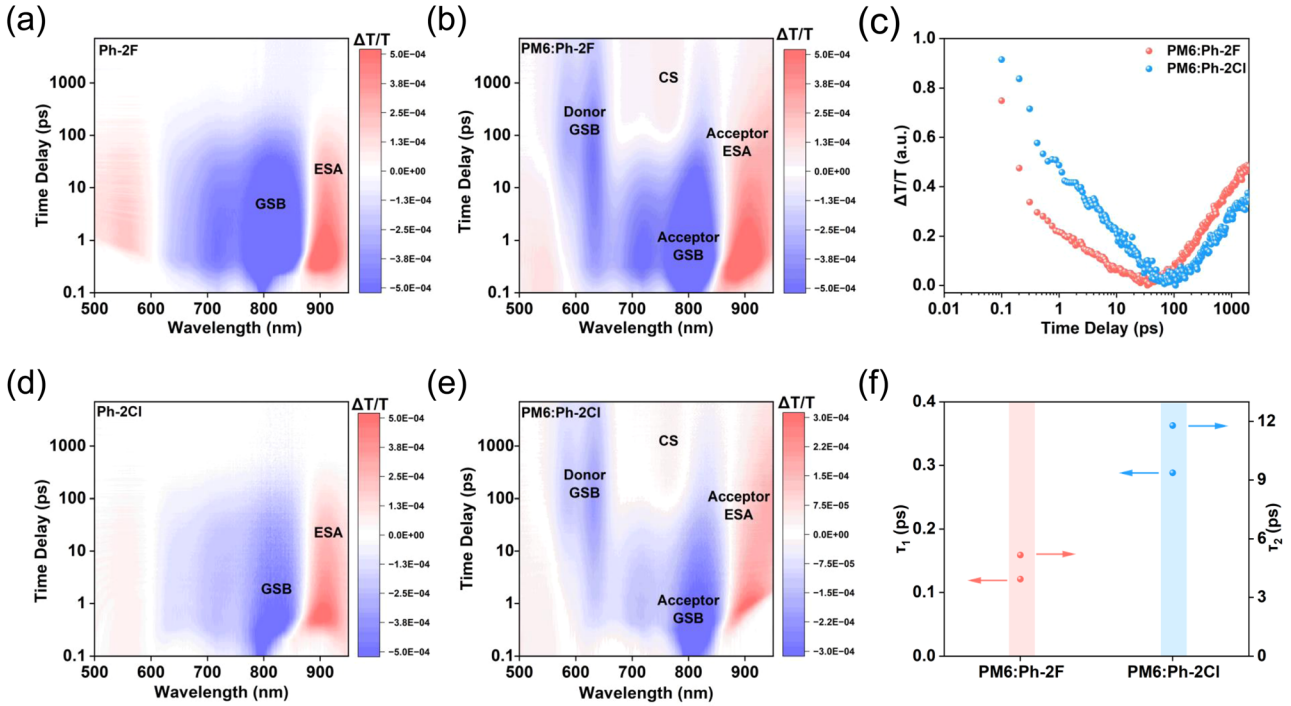

Fig. 3 Time-resolved two-dimensional (2D) femtosecond transient absorption spectra of (a) Ph-2F and (d) Ph-2Cl pristine film, optimized (b) PM6:Ph-2F and (e) PM6:Ph-2Cl blend films. (c) The trace kinetic curves of the donor GSB signal probed at 630 nm. (f) Exciton dynamics time acquired from fitting kinetic curves for PM6:Ph-2F and PM6:Ph-2Cl blend films.

Grazing-incidence wide angle X-ray scattering (GIWAXS) measurement was employed to investigate the effect of asymmetric molecular design strategy on molecular packing behavior and crystallization properties in the thin-film state, as shown in Fig. 4. The 1D line-cut profiles of the in-plane (IP) and out-of-plane (OOP) direction were extracted from the corresponding 2D patterns, and the detailed data are summarized in Tables S13 and S14. Both of the acceptors show obvious

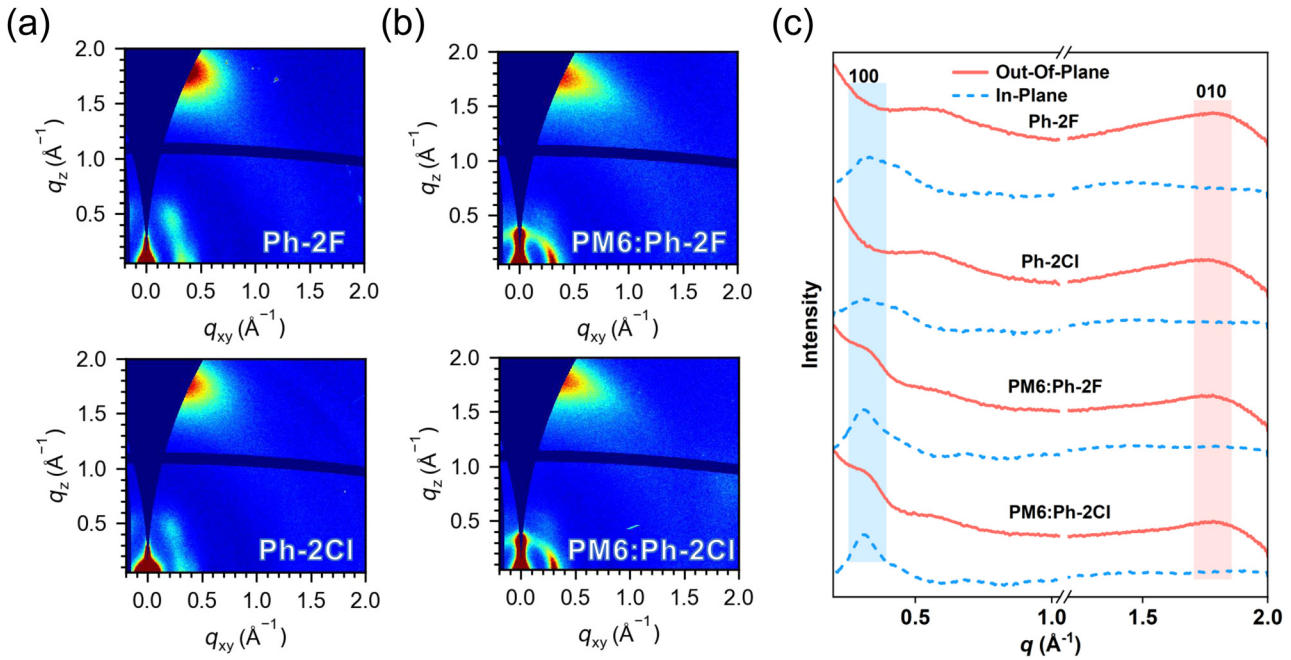

Fig. 4 2D GIWAXS patterns of (a) Ph-2F and Ph-2Cl pristine films and (b) optimized PM6:Ph-2F and PM6:Ph-2Cl blend films. (c) The line-cut profiles of in-plane (IP) and out-of-plane (OOP) orientation for the corresponding pristine and blend films.

face-on orientation in neat films, which is favorable for charge transfer along the vertical direction. The 1D linecut of the neat film shows that Ph-2F exhibits not only a smaller π–π packing distance of 3.53 Å accompanied with the (010) peak located at 1.78 $Å^{-1}$ but also a larger crystal coherence length (CCL) of 23.26 Å in the out-of-plane (OOP) direction compared with that of Ph-2Cl featuring a π–π packing distance of 3.61 Å and CCL value of 22.69 Å, indicating tighter and more well-ordered packing formed in the Ph-2F film, which was advantageous for facilitating charge transfer and resulting in higher electron mobility (Fig. S39 and Table S15). When blending with PM6, two blends can still maintain preferential face-on orientation. Although the two blends show the same *d*-spacing distance, the Ph-2F-based blend exhibits a larger CCL value of 31.23 Å than the Ph-2Cl-based one of 29.13 Å in the OOP direction, indicating the enhancement of π–π packing ordering and corresponding to the change tendency of blend charge mobilities. According to the reported work, a paracrystalline disorder factor (*g* factor) was introduced to quantify the ordering of the π–π packing peak in the blend film.[51] It is obvious that the Ph-2F-based blend exhibits a smaller g factor of 13.4% compared to the Ph-2Cl-based one of 13.9%. The larger CCL in the OOP direction and smaller g factor of the PM6:Ph-2F blend could be responsible for the enhanced charge transport properties and suppressed recombination behavior (Fig. S40), thus obtaining a high PCE in comparison with the PM6:Ph-2Cl-based blend.[52]

The blend film nanomorphology in OSCs plays an important role in determining charge transport properties and E_{loss}, thereby affecting photovoltaic efficiency.[53,54] As a result, atomic force microscopy (AFM) and contact angle test were applied to analyze the surface morphology and evaluate the miscibility between PM6 and acceptors, respectively. The root-mean-square roughness (R_q) is 0.91 nm for PM6:Ph-2F and 0.73 nm for PM6:Ph-2Cl, indicating both blends show relatively smooth and uniform surface morphology (Fig. 5). According to the phase images of the blend films, the Ph-2F-based blend exhibited an obviously clear bi-continuous interpenetrating fiber network, which facilitates charge transfer and suppresses recombination. The incorporation of infrared spectroscopy and AFM techniques can further clearly show phase separation, where the blue part represents the donor domain, and the red and yellow parts represent the domains containing acceptor. Note that PM6:Ph-2F exhibits more suitable phase separation than the PM6:Ph-2Cl blend film, which can form a greater D/A interface to accelerate exciton separation and transportation. The average fibril diameters extracted from AFM-IR patterns are displayed in Fig. S41 and S42, with average fibril diameters (extracted from AFM-IR linecut) of 10.99 nm for the Ph-2F-based blend and 18.77 nm for the Ph-2Cl-based blend. The larger fibril diameters formed in the Ph-2Cl-based blend can be mainly attributed to its over-aggregation property in the thin-film state, resulting in its oversized phase separation, while the Ph-2F-based blend with appropriate fiber size exhibits more evenly distributed fibers.

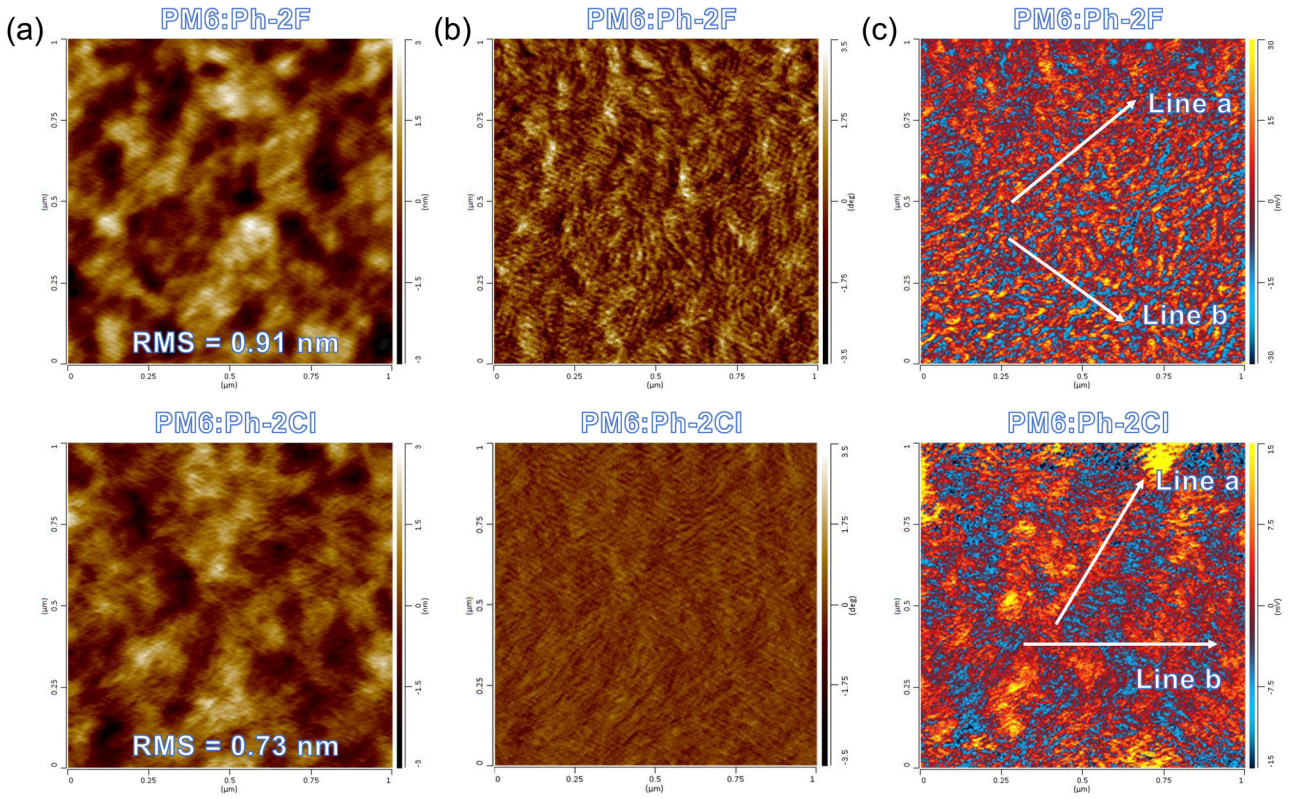

Fig. 5 AFM height images (a), phase images (b) and tapping AFM-IR images (c) for the optimized PM6:Ph-2F and PM6:Ph-2Cl blend films (1 μm × 1 μm), where a specific IR absorption at 2216 cm^{-1} for the CN group on the acceptor was used.

As shown in Fig. S43, the miscibility between donor and acceptor was closely associated with phase separation of the active layer, as evaluated by the Flory–Huggins interaction parameter (χ) calculated from the equation $\chi_{D:A} = K\left(\sqrt{\gamma_D} - \sqrt{\gamma_A}\right)^2$. Ph-2F exhibits smaller surface energies (γ) of 33.72 mN m^{-1} than those of 35.81 mN m^{-1} for Ph-2Cl, resulting in its reduced χ of 0.20 K compared with 0.39 K for Ph-2Cl (Table S16). The enlarged χ value of Ph-2Cl indicates its poor miscibility with PM6, which also explains the excessive self-aggregation behavior of Ph-2Cl in the AFM-IR images. In contrast, Ph-2F shows favorable miscibility with PM6, which ensures its proper phase separation in the blend film. Such favorable morphology formed in the PM6:Ph-2F blend can be attributed to the balanced crystallinity and miscibility, which is responsible for its enhanced charge mobilities and diminished recombination, eventually yielding better device performance. All the above results highlight the effectiveness of the asymmetric molecular design strategy in suppressing ΔE_3 and optimizing nanomorphology to improve exciton transport properties, thus enabling binary OSC efficiencies based on asymmetric acceptors exceeding 20%.

Conclusions

In summary, we demonstrated the effectiveness of combining core asymmetric substitution with halogenation engineering to design two high-performance acceptors, Ph-2F and Ph-2Cl. The synergistic effects of the asymmetric benzene-core substitution and halogenation not only suppressed non-radiative energy loss but also optimized nanomorphology. Specifically, the Ph-2F-based system exhibited optimized phase separation morphology, faster hole transfer dynamics, enhanced charge transport and reduced recombination. These factors collectively contributed to the simultaneous enhancement of J_{SC} and FF, while maintaining a high V_{OC}. As a result, an impressive PCE of 20.33% was achieved for the Ph-2F-based binary device. To the best of our knowledge, this efficiency is the highest value reported to date among the binary OSCs based on asymmetric acceptors. Furthermore, when the PM6:Ph-2F system was applied in the module, an impressive PCE of 17.16% was achieved, representing the highest value in binary OSC modules. Our findings highlight the significant potential of asymmetric acceptor design centered on core engineering to enhance device performance.

Author contributions

The synthesis studies were carried out by J. L., the two acceptors were characterized by J. L., and Z. S. carried out most of the device fabrication and measurement procedures. L. L. performed the large-area module experiments. W. Z. and G. L. carried out the theoretical computation and femtosecond transient absorption spectroscopy measurement of the two acceptors. X. W. and Y. C. supervised and directed this project. J. L. and X. W. wrote the manuscript. All authors discussed the results and commented on the manuscript.

Conflicts of interest

There are no conflicts to declare.

Data availability

The data that support the findings of this study are available from the corresponding author upon reasonable request.

Supplementary information including detailed synthesis procedure and characterization, device fabrication and related measurement results. See DOI: **https://doi.org/10.1039/d5ee03005f**

Acknowledgements

The authors gratefully acknowledge the Ministry of Science and Technology of China (2024YFF1401100 and 2023YFE0210400) and the financial support from the National Natural Science Foundation of China (52025033 and 52373189).

Notes and references

1 C. Yan, S. Barlow, Z. Wang, H. Yan, A. K. Y. Jen, S. R. Marder and X. Zhan, *Nat. Rev. Mater.*, 2018, **3**, 18003.
2 J. Hou, O. Inganäs, R. H. Friend and F. Gao, *Nat. Mater.*, 2018, **17**, 119–128.
3 S. Li, Z. Li, X. Wan and Y. Chen, *eScience*, 2023, **3**, 100085.
4 J. Zhang, H. S. Tan, X. Guo, A. Facchetti and H. Yan, *Nat. Energy*, 2018, **3**, 720–731.
5 G. Zhang, F. R. Lin, F. Qi, T. Heumüller, A. Distler, H.-J. Egelhaaf, N. Li, P. C. Y. Chow, C. J. Brabec, A. K. Y. Jen and H.-L. Yip, *Chem. Rev.*, 2022, **122**, 14180–14274.
6 G. Zhang, J. Zhao, P. C. Y. Chow, K. Jiang, J. Zhang, Z. Zhu, J. Zhang, F. Huang and H. Yan, *Chem. Rev.*, 2018, **118**, 3447–3507.
7 L. Meng, Y. Zhang, X. Wan, C. Li, X. Zhang, Y. Wang, X. Ke, Z. Xiao, L. Ding, R. Xia, H.-L. Yip, Y. Cao and Y. Chen, *Science*, 2018, **361**, 1094–1098.
8 S. Guan, Y. Li, C. Xu, N. Yin, C. Xu, C. Wang, M. Wang, Y. Xu, Q. Chen, D. Wang, L. Zuo and H. Chen, *Adv. Mater.*, 2024, **36**, 2400342.
9 R. Ma, B. Zou, Y. Hai, Y. Luo, Z. Luo, J. Wu, H. Yan and G. Li, *Adv. Mater.*, 2025, **37**, 2500861.
10 H. Chen, Y. Huang, R. Zhang, H. Mou, J. Ding, J. Zhou, Z. Wang, H. Li, W. Chen, J. Zhu, Q. Cheng, H. Gu, X. Wu, T. Zhang, Y. Wang, H. Zhu, Z. Xie, F. Gao, Y. Li and Y. Li, *Nat. Mater.*, 2025, **24**, 444–453.
11 C. Li, J. Song, H. Lai, H. Zhang, R. Zhou, J. Xu, H. Huang, L. Liu, J. Gao, Y. Li, M. H. Jee, Z. Zheng, S. Liu, J. Yan, X.-K. Chen, Z. Tang, C. Zhang, H. Y. Woo, F. He, F. Gao, H. Yan and Y. Sun, *Nat. Mater.*, 2025, **24**, 433–443.
12 Y. Jiang, K. Liu, F. Liu, G. Ran, M. Wang, T. Zhang, R. Xu, H. Liu, W. Zhang, Z. Wei, Y. Cui, X. Lu, J. Hou and X. Zhu, *Adv. Mater.*, 2025, **37**, 2500282.
13 L. Zhu, M. Zhang, G. Zhou, Z. Wang, W. Zhong, J. Zhuang, Z. Zhou, X. Gao, L. Kan, B. Hao, F. Han, R. Zeng, X. Xue,

S. Xu, H. Jing, B. Xiao, H. Zhu, Y. Zhang and F. Liu, *Joule*, 2024, **8**, 3153–3168.
14 P. Zhang, N. Gao, B. Du, Z. Xu, S. Wu, K. Zhu, X. Ma, H. Bin and Y. Li, *Angew. Chem., Int. Ed.*, 2025, **64**, e202424430.
15 H. Li, Y. Li, X. Dai, X. Xu and Q. Peng, *Angew. Chem., Int. Ed.*, 2025, **64**, e202416866.
16 X. Si, W. Shi, R. Wang, W. Zhao, Z. Suo, Z. Fu, G. Long, X. Hao, Z. Yao, X. Wan, C. Li and Y. Chen, *Nano Energy*, 2024, **131**, 110204.
17 J. Liu, R. Wang, L. Li, W. Zhao, Z. Suo, W. Shi, G. Long, Z. Yao, X. Wan and Y. Chen, *Energy Environ. Sci.*, 2025, **18**, 4470–4479.
18 D. Qiu, L. Zhang, H. Zhang, A. Tang, J. Zhang, Z. Wei and K. Lu, *J. Mater. Chem. A*, 2025, **13**, 4237–4246.
19 S. Li, L. Zhan, Y. Jin, G. Zhou, T.-K. Lau, R. Qin, M. Shi, C.-Z. Li, H. Zhu, X. Lu, F. Zhang and H. Chen, *Adv. Mater.*, 2020, **32**, 2001160.
20 C. He, Z. Chen, T. Wang, Z. Shen, Y. Li, J. Zhou, J. Yu, H. Fang, Y. Li, S. Li, X. Lu, W. Ma, F. Gao, Z. Xie, V. Coropceanu, H. Zhu, J.-L. Bredas, L. Zuo and H. Chen, *Nat. Commun.*, 2022, **13**, 2598.
21 S. Chen, S. Zhu, L. Hong, W. Deng, Y. Zhang, Y. Fu, Z. Zhong, M. Dong, C. Liu, X. Lu, K. Zhang and F. Huang, *Angew. Chem., Int. Ed.*, 2024, **63**, e202318756.
22 T. Li, K. Wang, G. Cai, Y. Li, H. Liu, Y. Jia, Z. Zhang, X. Lu, Y. Yang and Y. Lin, *JACS Au*, 2021, **1**, 1733–1742.
23 R. Sun, Y. Wu, X. Yang, Y. Gao, Z. Chen, K. Li, J. Qiao, T. Wang, J. Guo, C. Liu, X. Hao, H. Zhu and J. Min, *Adv. Mater.*, 2022, **34**, 2110147.
24 Z. Luo, R. Ma, T. Liu, J. Yu, Y. Xiao, R. Sun, G. Xie, J. Yuan, Y. Chen, K. Chen, G. Chai, H. Sun, J. Min, J. Zhang, Y. Zou, C. Yang, X. Lu, F. Gao and H. Yan, *Joule*, 2020, **4**, 1236–1247.
25 W. Gao, H. Fu, Y. Li, F. Lin, R. Sun, Z. Wu, X. Wu, C. Zhong, J. Min, J. Luo, H. Y. Woo, Z. Zhu and A. K. Y. Jen, *Adv. Energy Mater.*, 2021, **11**, 2003177.
26 H. Tian, Y. Luo, Z. Chen, T. Xu, R. Ma, J. Wu, G. Li, C. Yang and Z. Luo, *Adv. Energy Mater.*, 2025, **15**, 2404537.
27 C. Yang, Q. An, H.-R. Bai, H.-F. Zhi, H. S. Ryu, A. Mahmood, X. Zhao, S. Zhang, H. Y. Woo and J.-L. Wang, *Angew. Chem., Int. Ed.*, 2021, **60**, 19241–19252.
28 M. Saladina, P. Simón Marqués, A. Markina, S. Karuthedath, C. Wöpke, C. Göhler, Y. Chen, M. Allain, P. Blanchard, C. Cabanetos, D. Andrienko, F. Laquai, J. Gorenflot and C. Deibel, *Adv. Funct. Mater.*, 2021, **31**, 2007479.
29 H. Yao, D. Qian, H. Zhang, Y. Qin, B. Xu, Y. Cui, R. Yu, F. Gao and J. Hou, *Chin. J. Chem.*, 2018, **36**, 491–494.
30 C. He, Z. Bi, Z. Chen, J. Guo, X. Xia, X. Lu, J. Min, H. Zhu, W. Ma, L. Zuo and H. Chen, *Adv. Funct. Mater.*, 2022, **32**, 2112511.
31 Y. Gong, T. Zou, X. Li, S. Qin, G. Sun, T. Liang, R. Zhou, J. Zhang, J. Zhang, L. Meng, Z. Wei and Y. Li, *Energy Environ. Sci.*, 2024, **17**, 6844–6855.
32 K. Liu, Y. Jiang, G. Ran, F. Liu, W. Zhang and X. Zhu, *Joule*, 2024, **8**, 835–851.
33 Y. Cai, C. Xie, Q. Li, C. Liu, J. Gao, M. H. Jee, J. Qiao, Y. Li, J. Song, X. Hao, H. Y. Woo, Z. Tang, Y. Zhou, C. Zhang, H. Huang and Y. Sun, *Adv. Mater.*, 2023, **35**, 2208165.
34 W. Liu, S. Sun, L. Zhou, Y. Cui, W. Zhang, J. Hou, F. Liu, S. Xu and X. Zhu, *Angew. Chem., Int. Ed.*, 2022, **61**, e202116111.
35 C. M. Proctor, J. A. Love and T.-Q. Nguyen, *Adv. Mater.*, 2014, **26**, 5957–5961.
36 H. Liang, H. Chen, P. Wang, Y. Zhu, Y. Zhang, W. Feng, K. Ma, Y. Lin, Z. Ma, G. Long, C. Li, B. Kan, Z. Yao, H. Zhang, X. Wan and Y. Chen, *Adv. Funct. Mater.*, 2023, **33**, 2301573.
37 O. J. Sandberg, K. Tvingstedt, P. Meredith and A. Armin, *J. Phys. Chem. C*, 2019, **123**, 14261–14271.
38 A. Foertig, A. Baumann, D. Rauh, V. Dyakonov and C. Deibel, *Appl. Phys. Lett.*, 2009, **95**, 052104.
39 Y. Shi, Y. Chang, K. Lu, Z. Chen, J. Zhang, Y. Yan, D. Qiu, Y. Liu, M. A. Adil, W. Ma, X. Hao, L. Zhu and Z. Wei, *Nat. Commun.*, 2022, **13**, 3256.
40 J. Yao, T. Kirchartz, M. S. Vezie, M. A. Faist, W. Gong, Z. He, H. Wu, J. Troughton, T. Watson, D. Bryant and J. Nelson, *Phys. Rev. Appl.*, 2015, **4**, 014020.
41 U. Rau, U. W. Paetzold and T. Kirchartz, *Phys. Rev. B*, 2014, **90**, 035211.
42 J. Liu, S. Chen, D. Qian, B. Gautam, G. Yang, J. Zhao, J. Bergqvist, F. Zhang, W. Ma, H. Ade, O. Inganäs, K. Gundogdu, F. Gao and H. Yan, *Nat. Energy*, 2016, **1**, 16089.
43 K. Vandewal, K. Tvingstedt, A. Gadisa, O. Inganäs and J. V. Manca, *Nat. Mater.*, 2009, **8**, 904–909.
44 R. T. Ross, *J. Chem. Phys.*, 1967, **46**, 4590–4593.
45 T. Kirchartz, U. Rau, M. Kurth, J. Mattheis and J. H. Werner, *Thin Solid Films*, 2007, **515**, 6238–6242.
46 H. Chen, Y. Zou, H. Liang, T. He, X. Xu, Y. Zhang, Z. Ma, J. Wang, M. Zhang, Q. Li, C. Li, G. Long, X. Wan, Z. Yao and Y. Chen, *Sci. China: Chem.*, 2022, **65**, 1362–1373.
47 C. Li, J. Zhou, J. Song, J. Xu, H. Zhang, X. Zhang, J. Guo, L. Zhu, D. Wei, G. Han, J. Min, Y. Zhang, Z. Xie, Y. Yi, H. Yan, F. Gao, F. Liu and Y. Sun, *Nat. Energy*, 2021, **6**, 605–613.
48 X.-K. Chen, D. Qian, Y. Wang, T. Kirchartz, W. Tress, H. Yao, J. Yuan, M. Hülsbeck, M. Zhang, Y. Zou, Y. Sun, Y. Li, J. Hou, O. Inganäs, V. Coropceanu, J.-L. Bredas and F. Gao, *Nat. Energy*, 2021, **6**, 799–806.
49 Y. Jiang, S. Sun, R. Xu, F. Liu, X. Miao, G. Ran, K. Liu, Y. Yi, W. Zhang and X. Zhu, *Nat. Energy*, 2024, **9**, 975–986.
50 K. Liu, Y. Jiang, F. Liu, G. Ran, M. Wang, W. Wang, W. Zhang, Z. Wei, J. Hou and X. Zhu, *Adv. Mater.*, 2025, **37**, 2413376.
51 R. Zeng, M. Zhang, X. Wang, L. Zhu, B. Hao, W. Zhong, G. Zhou, J. Deng, S. Tan, J. Zhuang, F. Han, A. Zhang, Z. Zhou, X. Xue, S. Xu, J. Xu, Y. Liu, H. Lu, X. Wu, C. Wang, Z. Fink, T. P. Russell, H. Jing, Y. Zhang, Z. Bo and F. Liu, *Nat. Energy*, 2024, **9**, 1117–1128.
52 H. Tang, H. Chen, C. Yan, J. Huang, P. W. K. Fong, J. Lv, D. Hu, R. Singh, M. Kumar, Z. Xiao, Z. Kan, S. Lu and G. Li, *Adv. Energy Mater.*, 2020, **10**, 2001076.
53 S. Li, L. Zhan, N. Yao, X. Xia, Z. Chen, W. Yang, C. He, L. Zuo, M. Shi, H. Zhu, X. Lu, F. Zhang and H. Chen, *Nat. Commun.*, 2021, **12**, 4627.
54 L. Zhu, M. Zhang, J. Xu, C. Li, J. Yan, G. Zhou, W. Zhong, T. Hao, J. Song, X. Xue, Z. Zhou, R. Zeng, H. Zhu, C.-C. Chen, R. C. I. MacKenzie, Y. Zou, J. Nelson, Y. Zhang, Y. Sun and F. Liu, *Nat. Mater.*, 2022, **21**, 656–663.